Progress Report on Plane-Strain Tension Testing of ATF FeCrAl Cladding

Nuclear Technology Research and Development

Approved for public release.
Distribution is unlimited

Prepared for US Department of Energy
Advanced Fuel Campaign
B. Garrison
M. Gussev
K. Linton
Oak Ridge National Laboratory

M3FT20OR020206092
ORNL/SPR-2020/1631
August 2020

SUMMARY

Performance of advanced accident-tolerant fuel (ATF) claddings must be assessed under all relevant scenarios, including normal and off-normal operating conditions, as well as during a reactivity-initiated accident (RIA). During RIA, the fuel pellet may expand and cause significant loads on cladding, a condition known as *pellet cladding mechanical interaction* (PCMI), which may even lead to cladding failure. This report describes the fiscal year (FY) 2020 research activities and results from the development of separate-effects testing for ATF cladding candidate iron-chromium-aluminum (FeCrAl) tube specimens under loading conditions expected during RIA/PCMI events.

To assess material performance under PCMI, a high strain rate burst test, often termed the *modified burst test* (MBT), is commonly employed. However, execution of such a test in a hot cell requires significant research. To overcome the complexities of performing MBTs in a hot-cell environment on irradiated samples, a plane-strain tension (PST) test was proposed by several authors as an alternative approach for PCMI testing. A new fixture was developed so that PST specimens could be tested using a more accommodating design for hot-cell manipulators.

This report presents the PST fixture design, evaluates the possibility of modifying the specimen geometry, and discusses experimental results with unirradiated Al 6061 and FeCrAl tubes at various lengths. Furthermore, this report discusses the relevance and compatibility of the PST results to RIA scenarios and compares the PST and MBT results.

INTENTIONALLY BLANK

CONTENTS

FIGURES

TABLES

ACRONYMS

ATF	accident-tolerant fuel
DIC	digital image correlation
FeCrAl	iron-chromium-aluminum alloy
HFIR	High Flux Isotope Reactor
ID	inside diameter
LWR	light-water reactor
MBT	modified burst test
OD	outside diameter
ORNL	Oak Ridge National Laboratory
PCMI	pellet-cladding mechanical interaction
PST	plane strain tension
RIA	reactivity insertion accident
SEM	scanning electron microscope

ACKNOWLEDGMENTS

This work was supported by the US Department of Energy Office of Nuclear Energy Advanced Fuels Campaign. Dylan Richardson is acknowledged for technical discussions and help with complex SolidWorks drawings and assemblies.

1. INTRODUCTION

Accident-tolerant fuel (ATF) cladding candidates that have been designed to improve reactor safety during a severe design-basis loss of coolant accident must also improve or maintain current safety characteristics of light-water reactors (LWRs), including during a postulated reactivity-initiated accident (RIA) [1-2]. RIA scenarios include control rod ejection in pressurized water reactors and control rod drop in boiling water reactors, both of which cause a sudden increase of the fission-rate density in nuclear fuel. Some of the energy associated with the increased fission-rate density causes the fuel temperature to rapidly increase, and the fuel experiences isotropic thermal expansion. If the fuel-cladding gap closes during RIA, then further expansion of fuel induces mechanical strain on the cladding, a condition known as *pellet-cladding mechanical interaction* (PCMI) [3]. If the mechanical strain from PCMI is sufficient, then the cladding may rupture. Therefore, assessing the mechanical behavior of ATF cladding candidates during the PCMI phase of the RIA is vital for ensuring the safety of LWRs.

During the PCMI phase of RIA, the cladding undergoes specific mechanical loading conditions. Cladding tubes are expected to be under a multiaxial stress state at temperatures ranging from 275 to 800°C, and the millisecond-scale events induce strain rates of 1–5 s^{-1} [4]. Currently, separate-effects testing techniques, including the modified burst test (MBT) and the plane strain tension (PST) test, are being utilized and further developed to study these complex PCMI loads. MBT was introduced by the Electric Power Research Institute as a method to produce the multiaxial stress state under the high strain rates and temperature expected during RIA events. This method has been further developed by Oak Ridge National Laboratory (ORNL) [5–9]. The modified burst test implemented at ORNL includes the use of a servo hydraulic high-speed test frame, a high-speed camera, a precise mirror setup with a telecentric lens for digital image correlation (DIC) analysis [10], and insulated heating. The complexity of this method and data collection requires significant development for hot cell implementation. PST is a proposed alternative test for collecting PCMI-relevant mechanical performance data on irradiated LWR cladding geometries in a hot cell. PST was introduced by Pennsylvania State University [11] and is under development as part of this effort at ORNL. Successful development of the PST technique at ORNL should accomplish the following: (1) determine a simple, reliable way to measure specimen ductility during a PST test that can be implemented in hot cell, (2) evaluate how PST results agree with MBT results with respect to the strain-to-failure and fracture mechanisms, (3) evaluate the behavior of FeCrAl materials under complex stress/strain conditions (especially since most, if not all, of the previous PST work was done with Zircaloy-4 claddings), and (4) determine if there is a possibility to reduce specimen size, which is especially important when using irradiated material.

To support testing of irradiated ATF materials, neutron irradiations of vendor-led cladding concepts are being conducted using the High Flux Isotope Reactor (HFIR) at ORNL. HFIR flux trap irradiations are optimized by reducing the specimen size to accommodate the limited core space for irradiation experiments and to ensure the lowest possible activity levels of individual test specimens for post-irradiation examinations. The standard size of a PST specimen is 12 mm long. To improve the efficacy of PST specimen irradiations in HFIR, proportionally smaller PST specimens 6 and 3 mm in length were designed and tested, and the results were compared to those obtained using the standard size specimens.

This report presents an improved PST fixture design that can easily be used in a hot cell, discusses smaller PST specimen geometries (3 and 6 mm in length compared to the standard 12 mm length), and analyzes the test results of ORNL's ATF iron-chromium-aluminum (FeCrAl) alloys B136Y and C26M. Early analyses compared the PST results to those obtained in MBTs of the same materials.

2. MATERIALS AND METHODS

The material tested in this work was (1) nuclear-grade FeCrAl (C26M and B136Y) tubes developed at ORNL as ATF materials and (2) Al 6061 tubes used as a standard material. Their compositions are shown in Table 1. More details on the material can be found in the literature [12, 13].

Table 1. Chemical compositions of the alloys used in this work.

Alloy	Fe	Cr	Al	Mo	Si	Y	Other
C26M	Bal.	11.9	6.2	1.98	0.2	0.03	<0.01 C<0.005 S
B136Y	Bal.	12.99	6.14	<0.01	<0.01	0.003	0.0030 C, 0.0020 S, 0.0014 O, 0.0005 N
Al 6061	0.5	0.17	Bal.	-	0.69	-	0.0031 Cu, 0.0009 Mn, 0.0010 Zn, 0.0017Ti

These FeCrAl cladding alloys were used in previous ORNL MBT experiments [6, 8, 9], which allows for comparison of PST and MBT results. C26M had moderate strength level (estimated yield stress ~500–600 MPa) and reasonable ductility (total elongation ~20%). The first-generation B136Y alloy had slightly lower strength and larger ductility than the C26M cladding. Cladding tubes were produced in a collaboration between ORNL and commercial vendors. Al 6061 alloy was used as a model material; it had much lower strength than FeCrAl alloys, but it had a very similar ductility level. There is rich literature on this alloy—including research on mechanical behavior and fracture under complex stress states—which simplifies analysis and enhances understanding of the experimental results. The 12 mm PST specimen geometry was adopted from Link et al. [11]. This geometry and the shorter 6 and 3 mm specimens are shown in Figure 1. The lengths and widths of the notches were decreased proportionally as the tube length was shortened. PST tests using shorter tubes were performed on an MTS 2 kN Insight electromechanical test frame. The loads of the PST tests approached the load cell's maximum load, so further tests were performed on an Instron 5966. Based on specimen notch width, the nominal strain rate was held constant at 0.002 s^{-1} for all specimens. This corresponded to a crosshead displacement rate of 0.2 mm/s for 12 mm specimens, 0.1 mm/s for 6 mm specimens, and 0.05 mm/s for 3 mm specimens. Two setups should be considered when testing PST specimens: with notches oriented to the side in the 3 o'clock position, or with notches oriented toward the top of the mandrel in the 12 o'clock position. Both orientations are investigated in this report. Three tests were performed with C26M with each length at each position of (1) 6 mm length at 3 o'clock, (2) 6 mm at 12 o'clock, (3) 12 mm at 3 o'clock, and (4) 12 mm at 12 o'clock. One test was performed at each of the other material/length/orientation combinations. Tests were performed at room temperature, and two tests of 12 mm C26M were performed at 275°C—one at the 3 o'clock orientation, and one at 12 o'clock. Scanning electron microscope (SEM) images of the fracture surfaces were taken on a TESCAN MIRA3 SEM. Post-test specimen geometry measurements were taken on a Keyence VR-5000 Series.

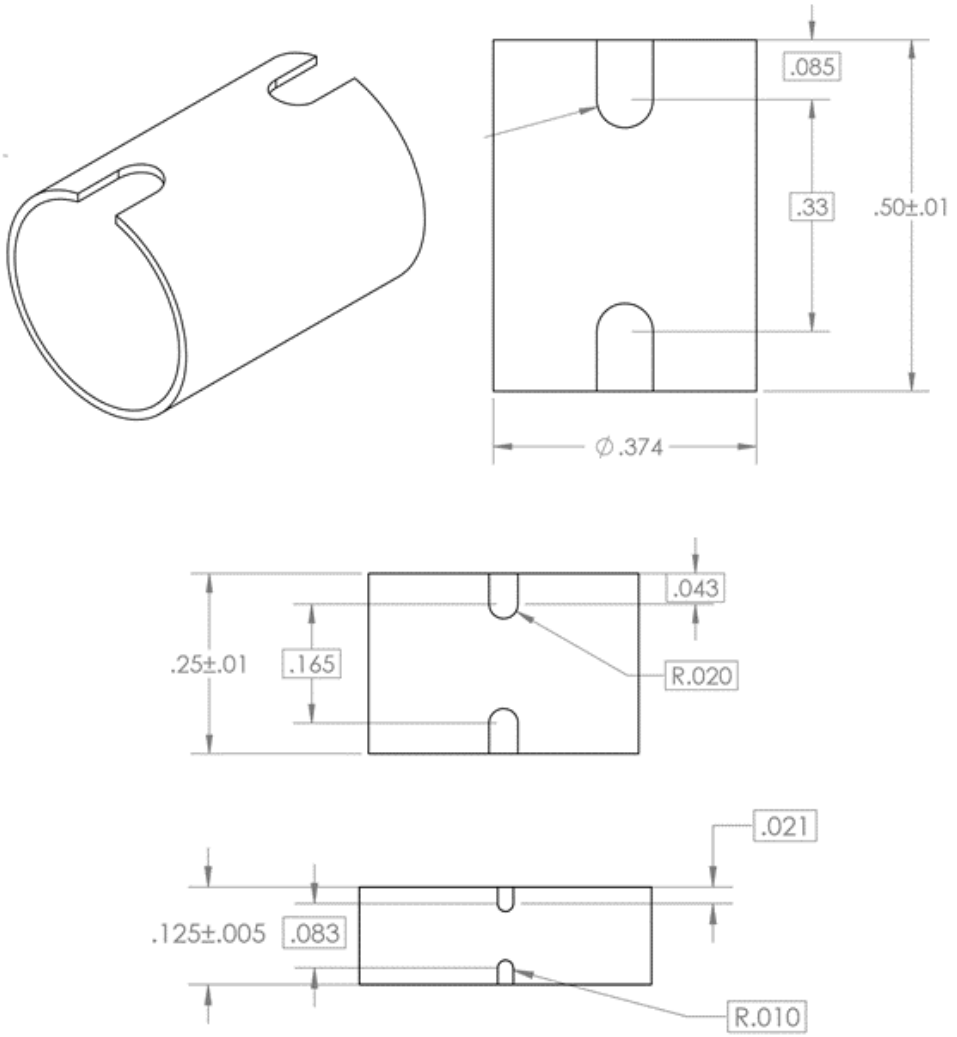

Figure 1. Drawings showing the isometric view and feature dimensions of the standard half-inch specimen (top image) and the dimensions of the proportionally smaller trial specimens (lower two images). Dimensions are in inches.

3. RESULTS AND DISCUSSION

3.1 PST FIXTURE DESIGN

The objective of the PST fixture design was to be able to test various cladding tube geometries in a hot cell. To accomplish this, the fixture should satisfy multiple requirements: (1) it must be able to withstand the loads from PST testing without damage, (2) it must have different options for the mandrel outside diameter (OD) to accommodate different tube inside diameters (IDs), and (3) it must remain compact and easy to use with the limited dexterity of hot cell manipulators. Based on the literature, PST tests were expected to reach loads above 5 kN due to high material strength and the friction between the specimen and fixture. However, the size of the mandrel insert is limited to allow it to fit inside the tube, posing a design challenge due to the limitation of the cross-sectional area of the mandrel. The fixture was designed to support the mandrel at both ends to endure the high loads, and the mandrel was designed as an inserted piece so it could be manufactured separately with a stronger material; stress concentrations were avoided where possible, and the other parts of the fixture were designed to distribute some of the load away from the mandrel. The insertion design of the mandrel also allows for a cost-effective method

to create different mandrels for different tube IDs. The fixture developed for PST testing is shown in exploded and assembled views in Figure 2.

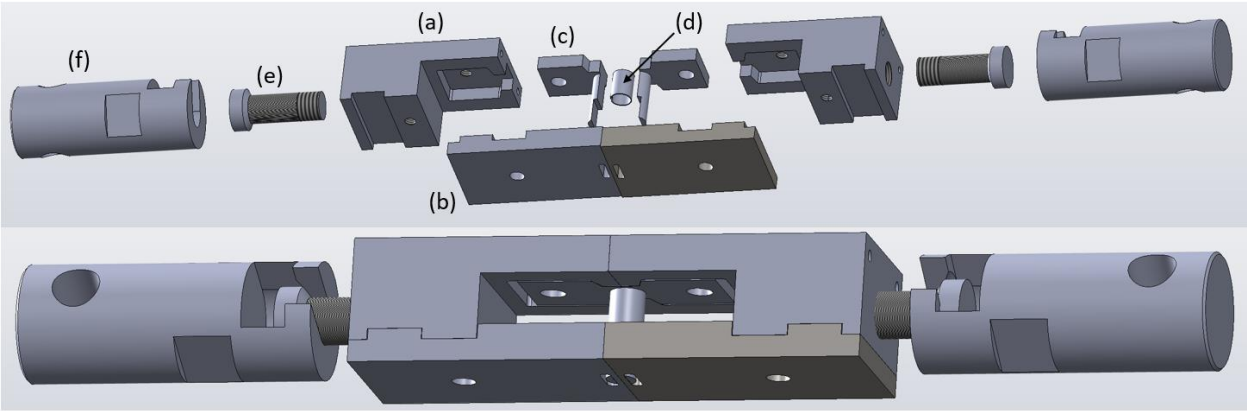

Figure 2. The exploded view (top) and assembled view (bottom) of the PST fixture showing the six main fixture components: (a) main grip piece, (b) lid, (c) mandrel insertion, (d) test specimen, (e) screw, and (f) screw-to-intron conversion piece. Despite the complex appearance, the fixture is easy to operate in the remote mode.

The fixture is made up of (a) the main grip piece (b) the lid, (c) the mandrel insertion, (d) the test specimen, (e) the screw, and (f), the screw-to-intron conversion piece. The main grip piece includes a shelf to distribute some of the stresses from the mandrel to the fixture body, two holes for alignment pins that restrict twisting during setup, a cubby for the mandrel insertions, and a threaded hole to connect the fixture to the load frame. The top of the screw slides into the gap of the helmet piece to make setup easier in a hot cell. The inside surface of the helmet piece and the screwhead surfaces are wedged so the fixture self-aligns to eliminate fixture and specimen bending. The other side of the helmet piece connects to the stock Instron pull rods. The mandrel inserts were manufactured with Rene 41 high-strength alloy, and the remaining parts were manufactured with 17-4 PH steel.

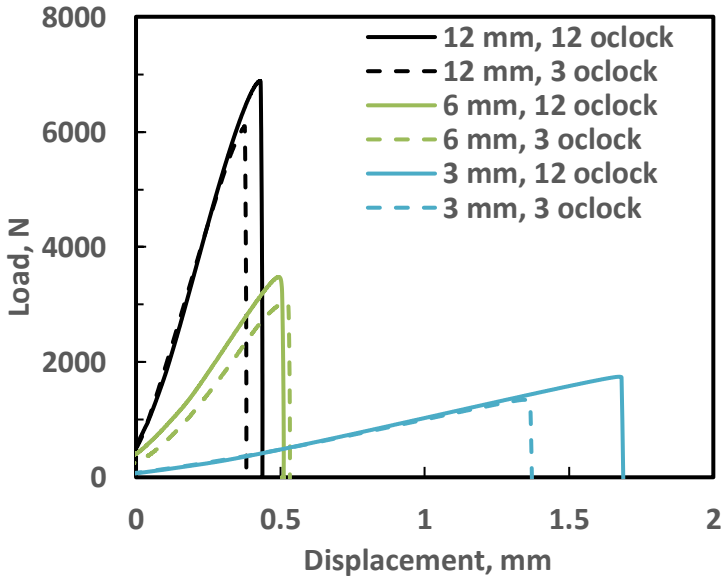

Figure 3. Representative load vs. displacement curves (one per condition) of C26M specimens of different lengths tested at room temperature at both notch orientations.

3.2 MECHANICAL TESTS AND ANALYSIS OF ENGINEERING TENSILE CURVES

Raw load vs. displacement tensile curves from the variable-length C26M PST specimens are shown in Figure 3. The figure shows that all curves have an elastic load region which is not completely straight; an increase in the slope can be seen due to the complexity of the experimental setup. Yielding and transition to the elastic-plastic behavior are clearly shown. The calculated maximum engineering stresses for C26M, B136Y, and Al 6061 materials of all three specimen lengths are shown in Figure 4. It was observed that the 12 mm length specimens at the 12 o'clock orientation reached loads close to 7 kN, which is likely caused by high friction between the specimens' inside surfaces and the mandrels. Furthermore, it was observed that the specimens tested at the 3 o'clock orientation also reached high loads, but they were consistently lower than their 12 o'clock counterparts. This is likely the result of limited friction force at the gage section, whereas at the 12 o'clock location, the gage section—the weakest part of the specimen—was experiencing contact friction.

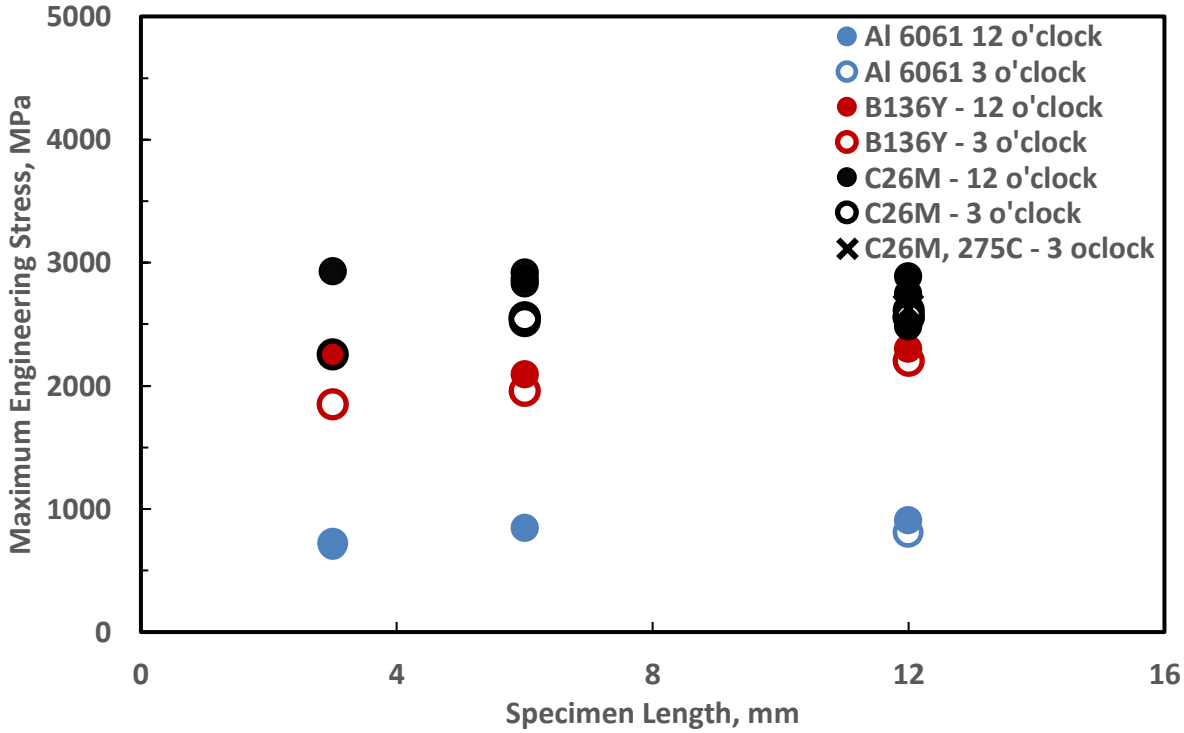

Figure 4. Nominal maximum engineering stress for each tested PST specimen calculated by dividing the maximum load (specimen stress plus frictional forces) by the nominal gage cross-sectional area.

Figure 4 shows the ultimate engineering stress calculated from the maximum load divided by the nominal cross-sectional area of each tube. Although these ultimate engineering stress values cannot be directly used as material properties because of the influence of friction and unknown true gage section, the scatter between curves is small, implying that the number of required tests for load-related calculations is small. Furthermore, the scatter among specimens of different lengths is within the scatter of specimens of the same parameters, so the possibility of using smaller PST specimens is not eliminated by this analysis. As expected, the specimens tested at the 3 o'clock orientation exhibited lower engineering stress values, which is largely attributed to their particular setup experiencing less friction.

The trend in which the ultimate engineering tensile strength of C26M is greater than B136Y, which is greater than that of aluminum, was clear from this analysis.

Because the loads are so high and the fixture is made of multiple parts, a large portion of the displacement comes from fixture/frame compliance. As a result, a processing technique to calculate plastic displacement (and therefore plastic engineering strain) was implemented to transform the displacement output into more realistic, useful mechanical properties. This technique was performed by removing the elastic strain from the total strain, because the majority of the fixture/frame compliance is in the elastic component. Figure 5 shows the results of applying this technique to calculate the maximum plastic strain or the plastic strain at failure. Maximum plastic strain calculations for 12 mm C26M specimens were 4.63 ± 1.77% for specimens at the 12 o'clock orientation and 1.91 ± 0.53 % for specimens tested at the 3 o'clock orientation, and the maximum plastic strain calculation for the C26M specimen tested at 275C at the 3 o'clock orientation failed at 1.5% plastic strain.

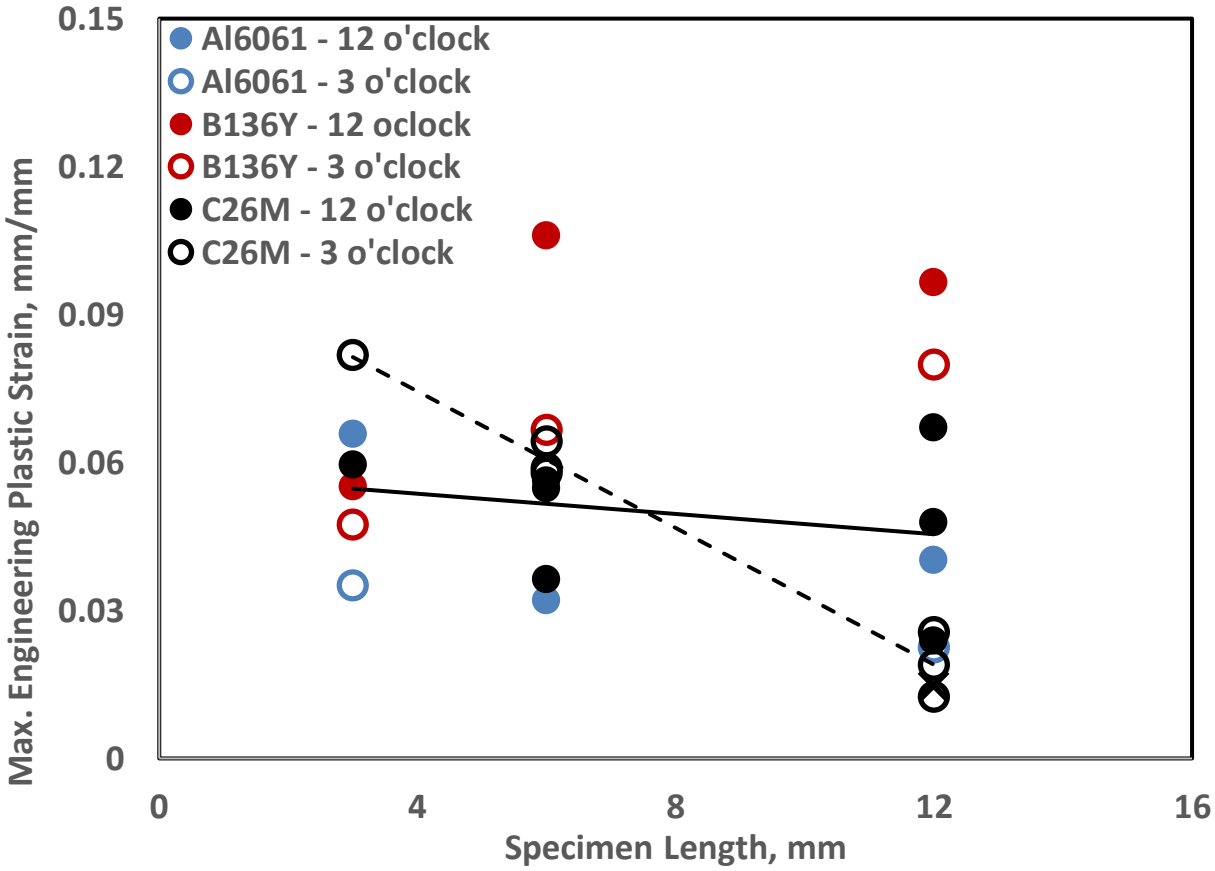

Figure 5. Nominal plastic strain at failure calculations for PST specimens performed in this work. The plastic strain was obtained by removing the elastic portion of the load/displacement data. Results for the specimen tested at 275C is in the expected range of failure strain compared to MBT total strain-to-failure results.

3.3 ANALYSIS OF STRAIN LOCALIZATION AND FRACTURE

Figure 6 shows post-test images of the shape of the failure region, with examples of 12 mm C26M specimens tested at the 12 o'clock orientation . These images were taken using the Keyence VR-5000 Series microscope. The remainder of the failure region images taken on the Keyence are included in Appendix A. It was observed that not every specimen failed in the same manner, with some specimens failing straight across the gage section along the notch symmetry (Figure 6b) while others failed off to the side (Figure 6a and 6c), sometimes traveling outside of the notched region. It should be noted that for the C26M specimens tested at the 12 o'clock orientation, the specimen that exhibited the highest plastic strain at failure and the least sudden load drop failed straight across the mid-gage, which is the expected PST failure mode from the literature. According to the literature, finite element analysis results indicate that the PST stress state activates in the middle of the gage section between the notches after sufficient plasticity is reached for specimens tested at the 3 o'clock location. Before that sufficient plasticity is realized, their results showed that tensile bands close to a uniaxial tensile stress state were present near the edges of the gage section while the middle of the gage section, where the PST stress state is eventually reached, is under compression. This tensile band/compression region state was said to be from initial bending of specimens tested at the 3 o'clock orientation as the gage section bends into the mandrels, but these results show that specimens tested at the 12 o'clock orientation also showed failure in the same location as those tensile bands [14, 15]. Currently, the mechanics that cause the failure in that location for the 12 o'clock location are unknown, so DIC calculations are recommended to further understand this result. The failure locations were mixed between the expected PST failure and tensile band location for both FeCrAl materials at varying lengths. The failure location for the aluminum specimens was the expected straight-across failure, which is in agreement with the PST state forming after sufficient plasticity, and it further suggests that aluminum may be more sensitive to ductility loss from stress biaxiality than the FeCrAl materials. Furthermore, for both FeCrAl materials, some deformation bands (see Figure 6b and Appendix A) could be observed on the specimen's surface outside the failure region. These features were also observed in MBT specimens. Epoxy-mounting some specimen cross sections might allow for measurement of these features and comparison with the two tests and materials.

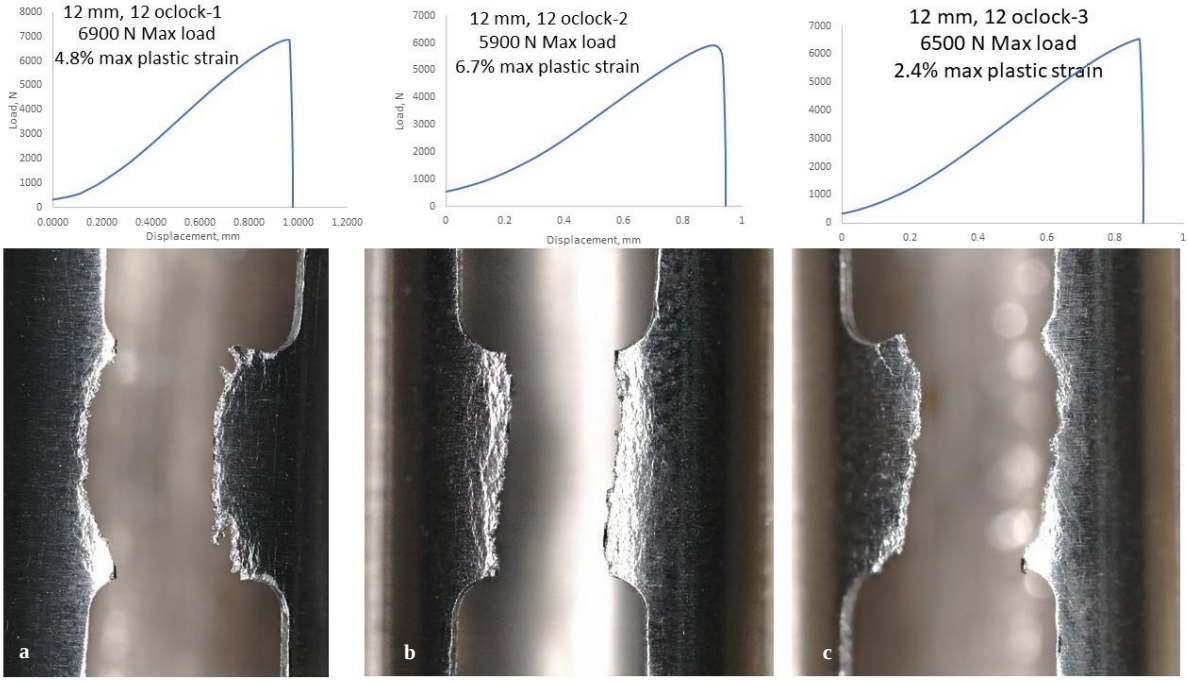

Figure 6. Keyence images of the shape of failure for 12 mm length C26M specimens tested at the 12 o'clock orientation. Pronounced slip lines and deformation bands can be observed.

3.4 AN APPROACH TO MEASURE THE STRAIN-TO-FAILURE VALUE

The Keyence microscope was also used to take optical images of the failure cross-sections of each specimen, and the wall thickness at the middle of the gage section was measured using the Keyence software. An example of an image and illustration of how the thickness was measured is shown in Figure 7 below. The middle of the gage section is expected to be in PST, where the hoop strain is the major strain, the through-thickness strain is the minor strain, and the axial strain is close to zero. The wall thickness at the middle of the gage section was measured and compared to the measured wall thickness at the outside of the gage region (assumed to be undeformed). This value, which measured the minor plastic strain can potentially be used as a material performance evaluation. The results of this procedure for all specimens is shown in Figure 8. For the three 12 mm length C26M specimens tested at each orientation, the wall thickness reduction was 9.4% ± 6.8 for the 12 o'clock orientation and 10.6% ± 4.8 for the 3 o'clock orientation. These strain values are in a realistic range, but the scatter is exceptionally large. It is also of note that the scatter in 6 mm specimens was significantly lower (±0.85 for the 12 o'clock orientation and ±1.95 for the 3 o'clock orientation) for the 3 specimens tested at each orientation. Like the plastic strain calculations, results from this analysis also showed a small length dependence of PST specimens, with 12 o'clock orientation specimens showing less sensitivity than their 3 o'clock counterparts. Moreover, other than the 3 mm specimens, B136Y showed more plastic deformation than the C26M specimens, which is similar to the MBT result, and the aluminum specimens were shown to be significantly less ductile than expected.

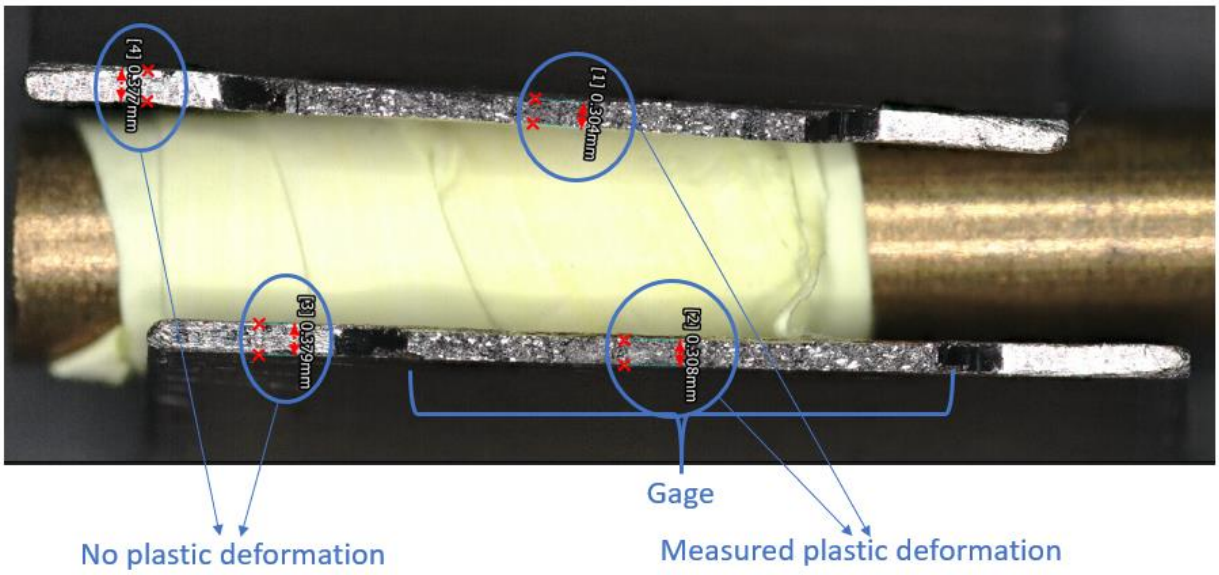

Figure 7. Image taken on the Keyence microscope of the post-test PST specimen cross section. The average wall thickness at the center of the gage (this area was deformed under plane strain conditions) was compared to the original tube wall thickness to determine the reduction in cross section from the PST experiment.

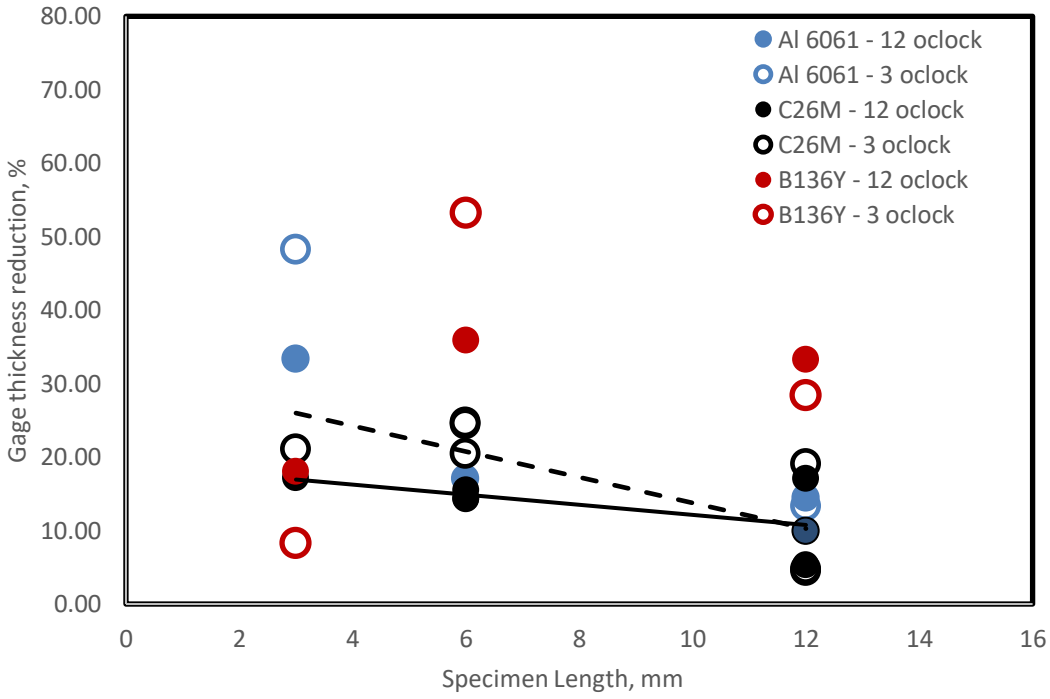

Figure 8. Results from measuring the wall thickness reduction of PST specimens in this work.

3.5 ANALYSIS OF FRACTURE MECHANISMS

SEM images of the 12 mm 3 o'clock C26M specimen tested at 275°C and the MBT specimen tested at 275°C are shown in Figure 9 below. Both specimens exhibited ductile failure, which is indicated by visible voids on the surfaces and thinning of the wall to a knife-like edge. This is a promising result that supports the comparability of MBT and PST test results. The 12 mm specimens of each material tested at the 12 o'clock orientation at room temperature are shown in Figure 10 below. It was found that both FeCrAl materials failed in a brittle manner at room temperature, and the aluminum specimens failed in a ductile manner, with visible voids present. This suggests that there is a ductile-to-brittle transition temperature between room temperature and 275°C for FeCrAl materials and that translating room temperature results to MBT/RIA scenarios is difficult.

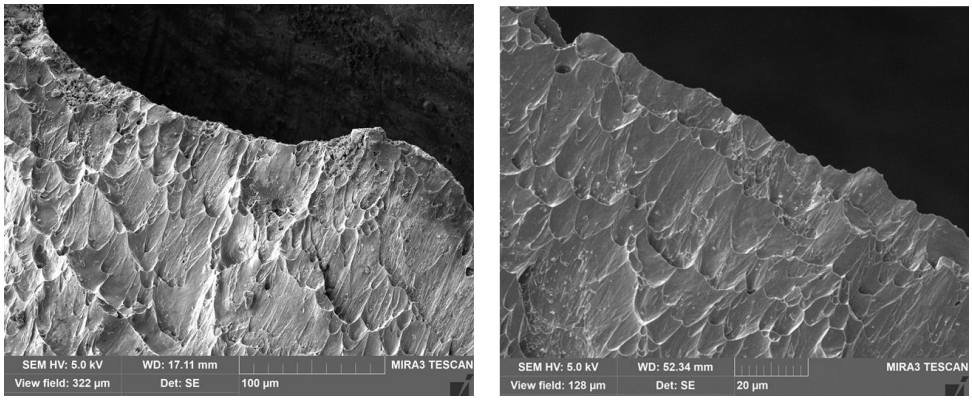

Figure 9. SEM images: MBT failure of C26M at 275°C (left), and PST failure of C26M at the 3 o'clock orientation at 275°C (right). The elongated dimples and void features in both images indicate ductile fracture.

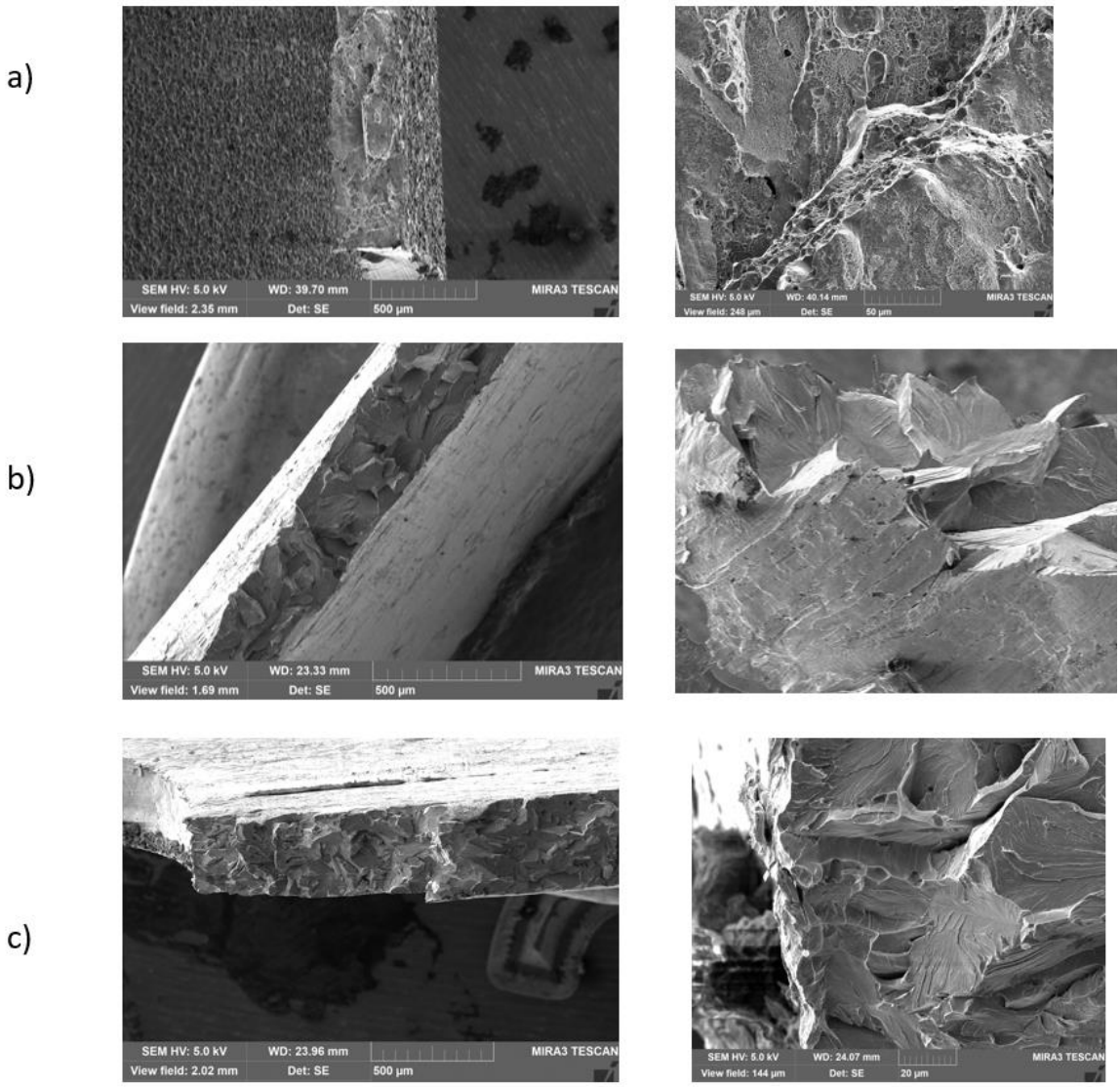

Figure 10. SEM images of the failure regions of 12 mm, 12 o'clock specimens of (a) Al 6061, (b) B136Y, and (c) C26M materials tested at room temperature. The FeCrAl materials showed brittle fracture (cleavage surface), whereas the Al 6061 material showed mostly ductile fracture mechanism.

One 275°C test was performed with the C26M 12 mm length specimen at the 12 o'clock location, but its results were not included in the previous data because the specimen did not fail in the gage section. This result is shown below in Figure 11. This result may have been caused by tube quality or loosened connections in the fixture during heating. More tests are required to completely understand this failure mode.

3.6 COMPARISON OF PST AND MBT RESULTS

As mentioned in the introduction, PST testing may be considered a reliable replacement of MBT, but only if it reproduces the mechanical behavior during MBT and provides comparable strain-to-failure

values. Although it is difficult to make the final conclusion regarding PST testing, the present work yielded some preliminary results to open the discussion and evaluate a general feasibility of such a replacement.

Considering that the recent MBT results with C26M at 275°C exhibited failure strains in the 2–4% range, the plastic strain value calculated here is a promising result for PST's ability to complement MBT results. Furthermore, the plastic strain values calculated for 12 mm B136Y specimens were 9.7 and 8.0%, which is also promising, as they compare to the MBT failure strains in the 4 to 8% range.

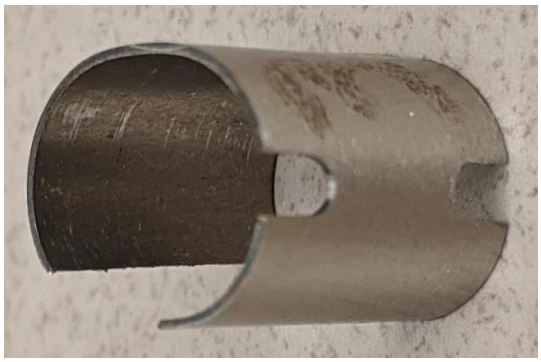

Figure 11. Twelve mm long C26M specimen tested at 275°C at the 12 o'clock orientation that did not fail at the specimen gage, suggesting a manufacturing defect or a nonmetallic inclusion.

However, it should be noted that (1) the MBTs were performed at 275°C, whereas the PST tests were performed at room temperature, and (2) the MBT strain values are the total strain value (the elastic and plastic strain together), whereas the PST strains calculated in this manner only include plastic strain. With that in mind, the expectation is that plastic strain calculations would be less than the total strain, which is consistent for the single high-temperature result.

More high-temperature testing is recommended to understand the scatter, but considering the small scatter in the 3 o'clock specimens, the volume of tests probably does not need to exceed 3 specimens. Furthermore, implementing DIC in the future to directly measure the surface total strains of C26M PST specimens is recommended to better compare the results to the total strain calculations of MBT materials.

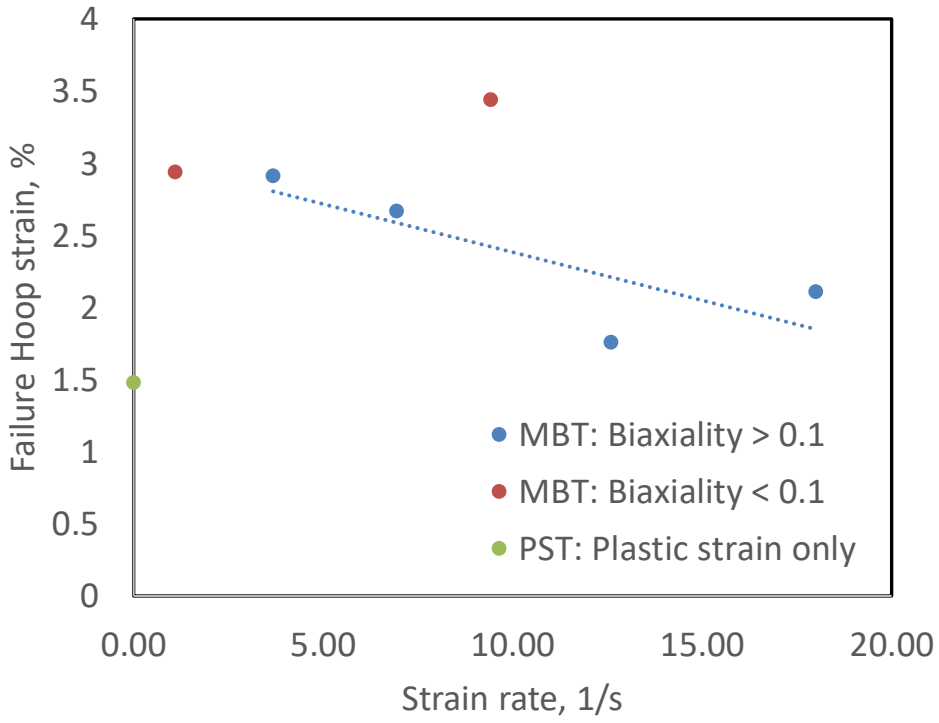

Figure 12. Total strain calculations from MBTs with C26M material tested at 275°C compared to the plastic strain calculated from a 12 mm C26M PST test at the 3 o'clock orientation. Strains from thickness reductions (5–17 %) appear to be out of the expected range from MBT (2–4 %).

Also of note, the results among different-length specimens show that there is a large sensitivity to specimen length for specimens tested at the 3 o'clock orientation, but the sensitivity is within the scatter for specimens tested at the 12 o'clock orientation. This is partly due to the larger scatter among specimens with all the same parameters. A higher volume of testing is recommended, along with the inclusion of DIC measurements, to determine whether shorter length specimens tested at the 12 o'clock orientation are viable replacements for 12 mm specimens. Aluminum 6061was expected to be more ductile than both the FeCrAl materials, but it showed comparable plastic strains at failure. The reason behind this low plasticity is unknown at this time, but perhaps aluminum is more sensitive to ductility loss at higher stress biaxialities.

4. CONCLUSIONS AND FUTURE WORK

- **A new, compact, hot cell–suitable fixture to test PST specimens was developed,** and multiple PST tests were successfully performed with two ORNL ATF FeCrAl concepts—B136Y and C26M alloys. A high temperature test was also successfully completed.
- **SEM fractography analysis showed that PST testing accurately reproduces fracture mechanisms observed in the MBT.** For instance, C26M specimens tested at 275°C showed ductile failure mechanisms for both PST tests and MBTs, whereas room temperature tests showed brittle failure in C26M, suggesting a ductile-to-brittle transition temperature between room temperature and 275°C. Additionally, it was found that some specimens failed straight across the gage region, while other specimens' failure paths were off to the side, sometimes existing outside of the gage region entirely. There was no discernable pattern between failure shapes other than Al showing all straight-across failures, whereas the FeCrAl materials had a mixture of both failure shapes.
- **Smaller (shorter) geometries were investigated but were finally rejected.** Plastic strain calculations and wall thickness reduction measurements both showed that 12 mm specimens exhibited lower plasticity than the shorter specimens, so the longer specimens were determined to be the conservative specimen geometry. The same trend was also observed in the Al 6061 specimens, but B136Y alloy tubes revealed more complex behavior.
- **Wall thickness measurements were employed to provide the strain-to-failure values for PST specimens. This approach provides an acceptable outcome.** Due to high friction and unavoidable fixture/frame compliance, direct conversion of common load/displacement output (e.g., raw deformation curves) to broadly useful material properties is not possible.
- **Comparison of the PST and MBT results for C26M alloy at 275°C showed that PST provided a plastic strain to failure that is comparable to that of MBT, but strain-to-failure values determined from wall thickness reductions were higher than the values for MBT.** This result compares the plastic strain calculated from PST test data to the total strain from MBT results, which requires more work to fully verify. Plastic strain calculations with room temperature tests at 3 o'clock did not show significantly different values than the high-temperature result, and tests at the 12 o'clock orientation showed significantly more ductility, far surpassing the expected value from MBT. Similarly, strain values from wall thickness reductions showed higher strain to failure than the values from MBT in tests performed at both orientations. The reason is not clear at this writing: it may be related to the strain rate effect or some differences in the stress/strain state between the MBT and PST specimens. As this factor is critical in the context of the present work, this aspect requires more work.

The following tests are recommended in the future to enhance this work:

1. Employ common (in-situ or post-test, painted or engraved pattern) DIC strain measurements of the surface strains to compliment the plastic strain calculations, experimentally determine the strain state at failure for tests that fail outside the middle of the gage, and shed some light on the rejected high temperature 12 o'clock specimen. This could provide results that are in better

agreement with the MBT results and could validate the hot cell–applicable methods tested in this work.

2. Evaluate alternate loading schemes to minimize friction, which has the potential to disturb the stress state and cause deviations from desirable plane-strain behavior.
3. Perform more high-temperature tests and more tests at an increased strain rate.

5. REFERENCES

[1] S. Zinkle, K. Terrani, J. Gehin, L. Ott and L. Snead, "Accident Tolerant Fuels for LWRs: A Perspective," *Journal of Nuclear Materials* 448, pp. 374–379, 2014.

[2] K. Terrani, "Accident Tolerant Fuel Cladding Development: Promise, Status, and Challenges," *Journal of Nuclear Materials* 501, pp. 13–30, 2018.

[3] T. Alam, M. Khan, M. Pathak, K. Ravi, R. Singh and S. Gupta, "A Review on the Clad Failure Studies," *Nuclear Engineering and Design* 241, pp. 3658–3677, 2011.

[4] P. Rudling, L. Jernkvist, F. Garzarolli, R. Adamson, T. Mahmood, A. Strasser and C. Patterson, *Nuclear Fuel Behavior under RIA Conditions*, A. N. T. International, Molnlycke, Sweden, 2016.

[5] M. N. Cinbiz, N. Brown, R. Lowden, K. Linton and K. Terrani, *RIA Simulation Tests Using Driver Tube for ATF Cladding*, ORNL/SR-2017/346, ORNL, Oak Ridge, Tennessee, 2017.

[6] M. N. Cinbiz, N. Brown, R. Lowden, M. Gussev, K. Linton and K. Terrani, *Report on Design and Failure Limits of SiC/SiC and FeCrAl ATF Cladding Concepts under RIA*, ORNL/LTR-2018/521, ORNL, Oak Ridge, Tennessee, 2018.

[7] M. N. Cinbiz, M. Gussev, K. Linton and K. Terrani, "An Advanced Experimental Design for Modified Burst Testing of Nuclear Fuel Cladding Materials during Transient Loading," *Annals of Nuclear Energy* 127, pp. 30–38, 2019.

[8] M. N. Cinbiz, B. Garrison, R. Lowden, R. Sitterson and K. Linton, *Progress Report on Modified Burst Testing and Alternative Test Methodologies*, ORNL/SPR-2019/1129, ORNL, Oak Ridge, Tennessee, 2019.

[9] N. Brown, B. Garrison, R. Lowden, M. Cinbiz and K. Linton, "Mechanical Failure of Fresh Nuclear Grade Iron-Chromium-Aluminum (FeCrAl) Cladding under Simulated Hot Zero Power Reactivity Initiated Accident Conditions," *Journal of Nuclear Materials* 539, 2020.

[10] J. Blaber, B. Adair and A. Antoniou, "Ncorr: Open-Source 2D Digital Image Correlation," *Experimental Mechanics* 55, pp. 1105–1122, 2015.

[11] T. Link, D. Koss and A. Motta, "Failure of Zircaloy Cladding under Transverse Plane-Strain Deformation," *Nuclear Engineering and Design* 186, pp. 379–394, 1998.

[12] Z. T. Thompson, K. Terrani and Y. Yamamoto, "Elastic Modulus Measurement of ORNL ATF FeCrAl Alloys," ORNL/TM-2015/632, ORNL, Oak Ridge, Tennessee, 2015.

[13] K. Field, M. Snead, Y. Yamamoto and K. Terrani, "Handbook on the Material Properties of FeCrAl Alloys for Nuclear Power Production Applications," ORNL/SPR-2018/905, ORNL, Oak Ridge, Tennessee, 2018.

[14] S. Carassou, M. Le Saux, J. P. Pizzanelli, O. Rabouille, X. Averty, C. Poussard, B. Cazalis, J. Desquines and C. Bernaudat, "Ductility and Failure Behaviour of Both Unirradiated and Irradiated Zircaloy-4 Cladding Using Plane Strain Tensile Specimens" (NEA-CSNI-R–2010-7), Nuclear Energy Agency of the OECD (NEA), 2010.

[15] J. Desquines, D. Koss, A. Motta, B. Cazalis and M. Petit, "The Issue of Stress State during Mechanical Tests to Assess Cladding Performance during a Reactivity-Initiated Accident (RIA)," *Journal of Nuclear Materials* 412, pp. 250–267, 2011.

APPENDIX A. FAILURE REGION IMAGES TAKEN ON THE KEYENCE

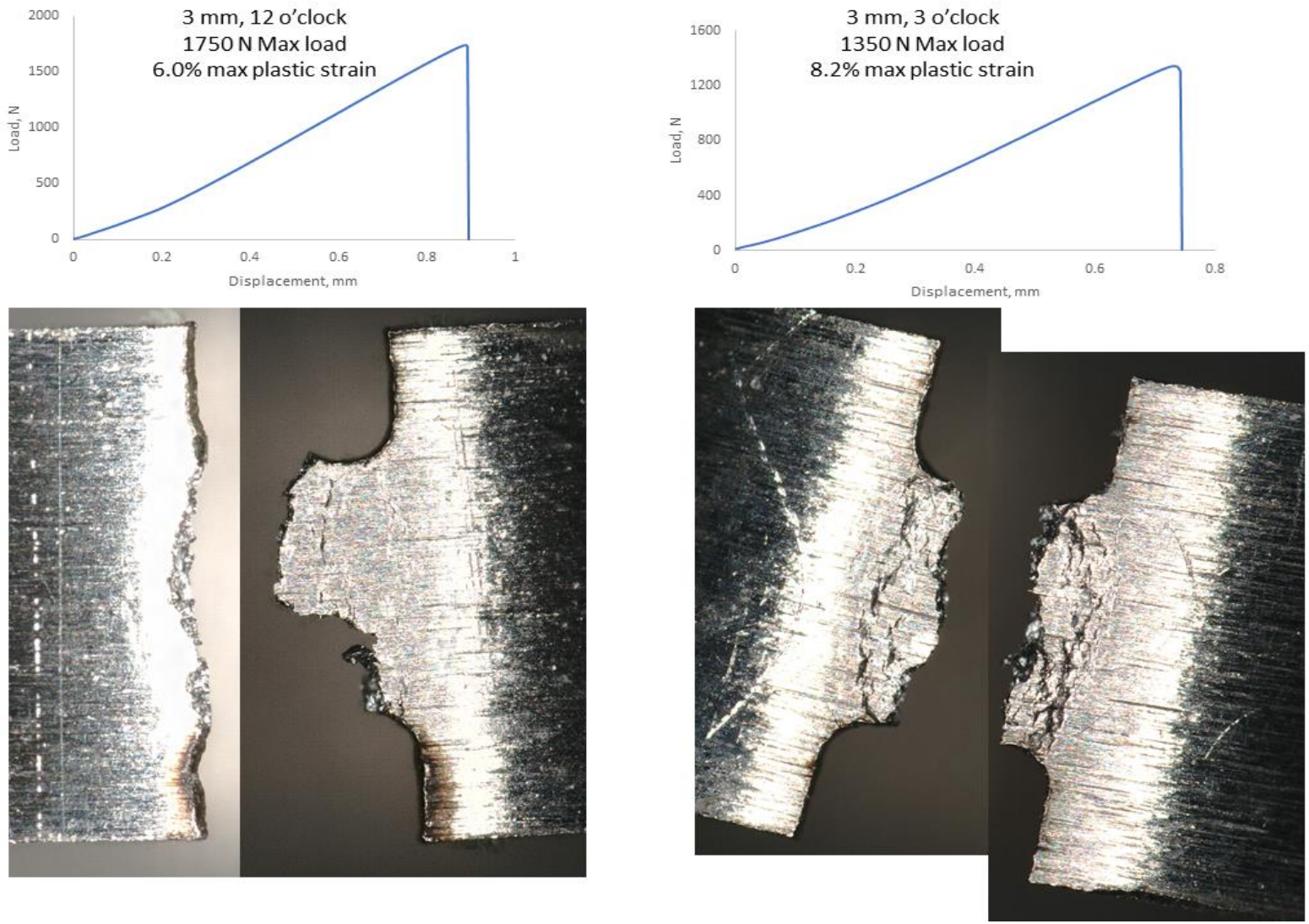

Figure A-1. Gage shape and mechanical test data for 3 mm C26M specimens tested at the 12 o'clock (left) and 3 o'clock (right) orientations.

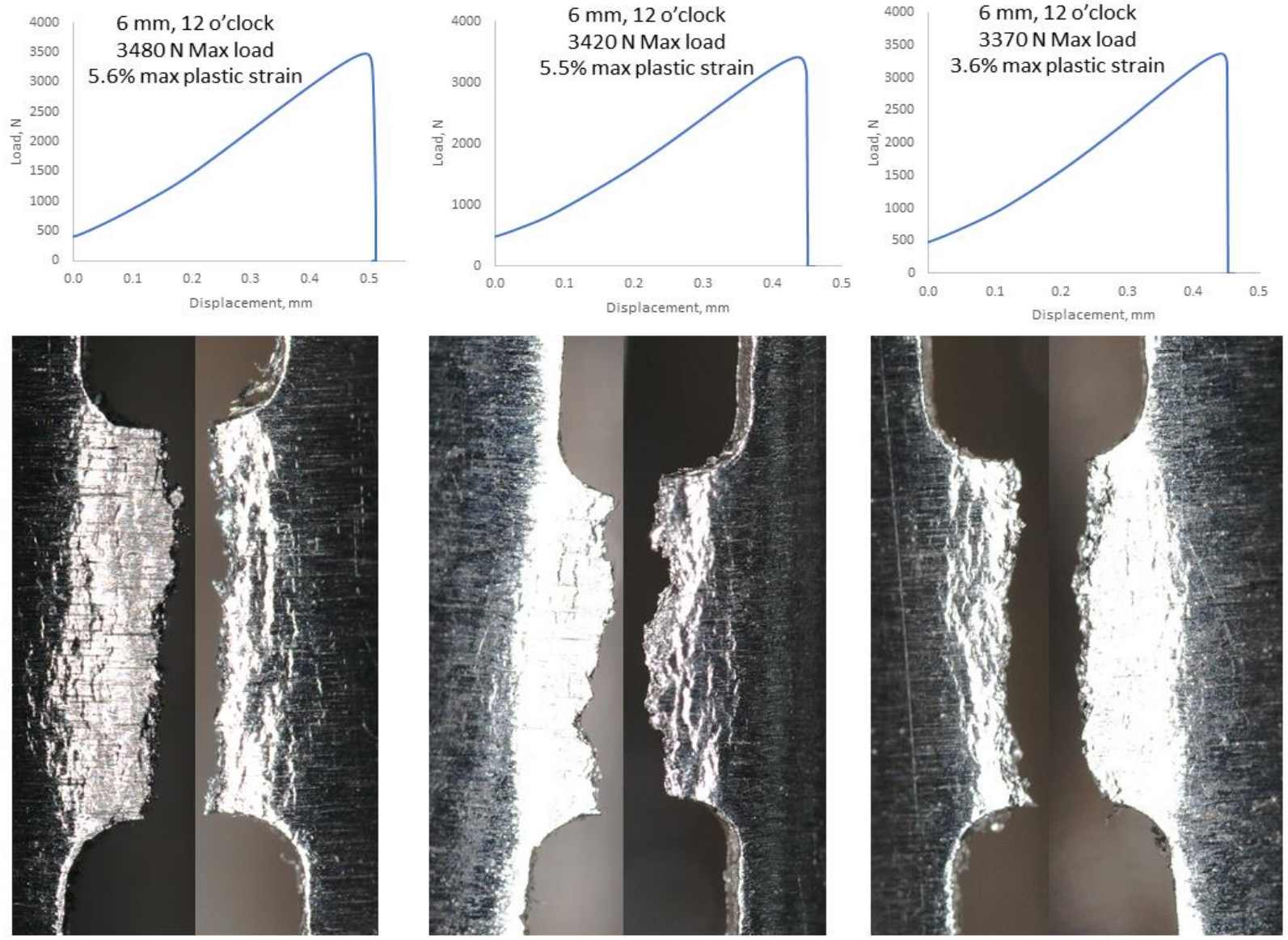

Figure A-2. Gage shape and mechanical test data for 6 mm C26M specimens tested at the 12 o'clock orientation.

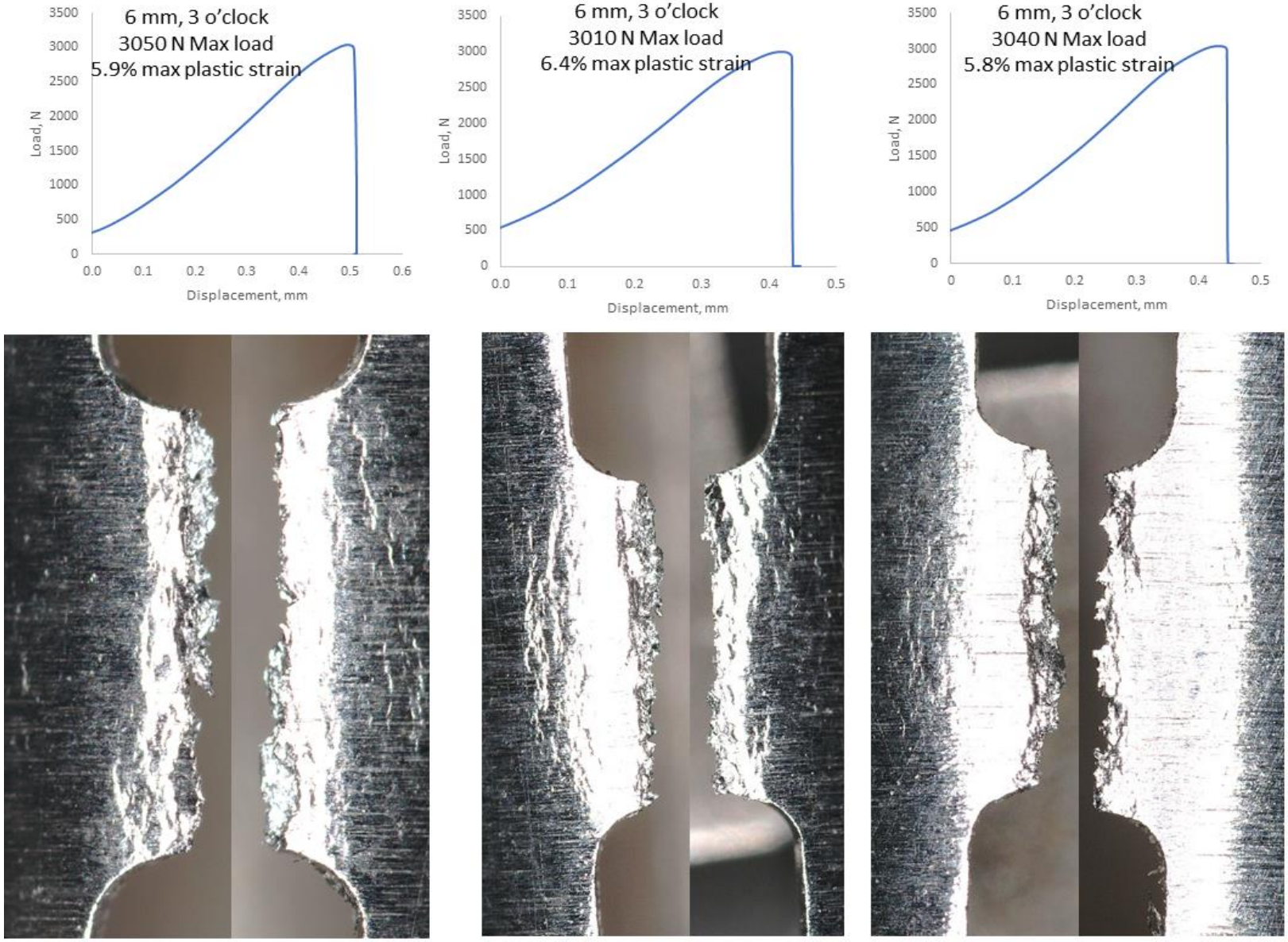

Figure A-3. Gage shape and mechanical test data for 6 mm C26M specimens tested at the 3 o'clock orientation.

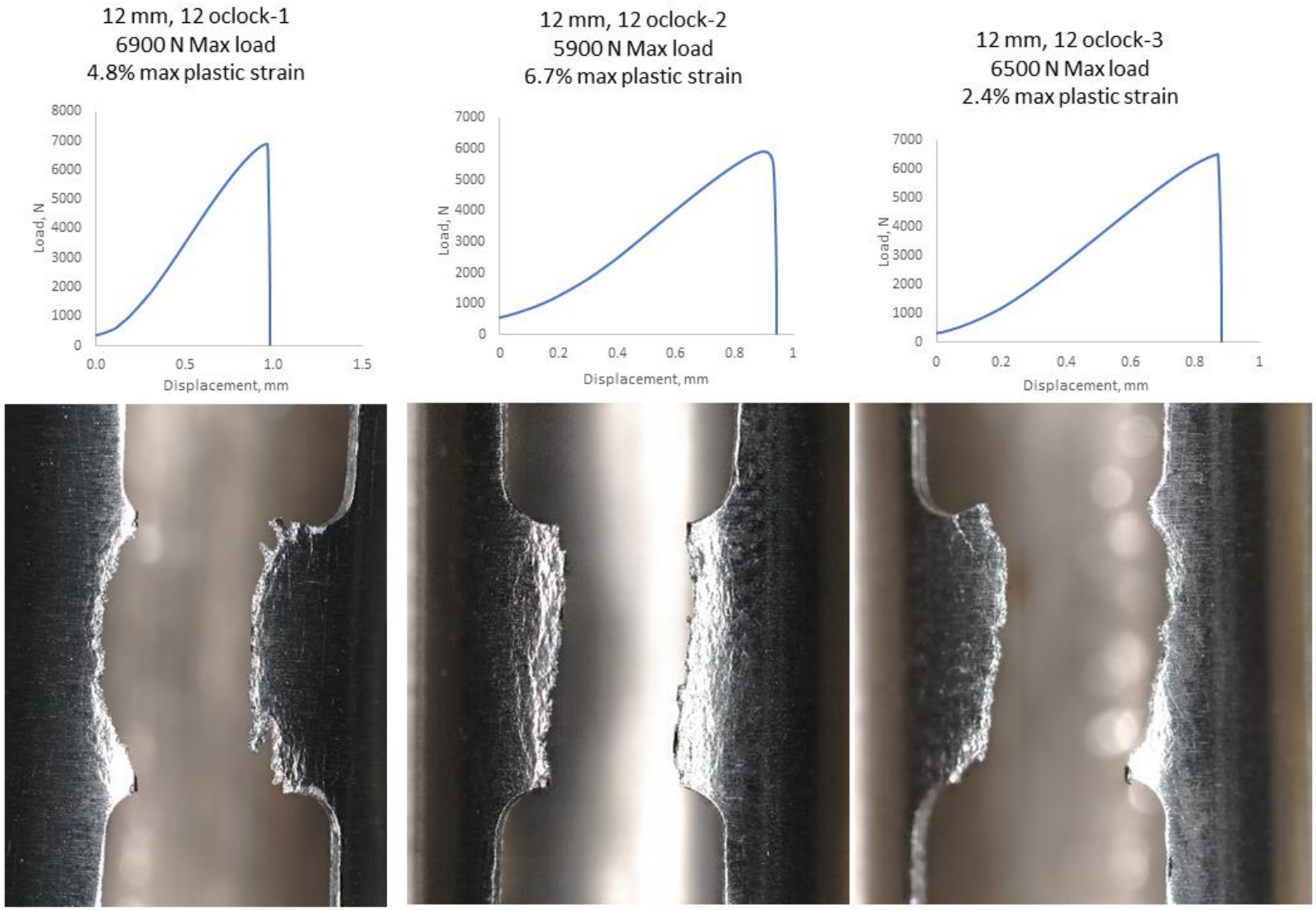

Figure A-4. Gage shape and mechanical test data for 12 mm C26M specimens tested at the 12 o'clock orientation.

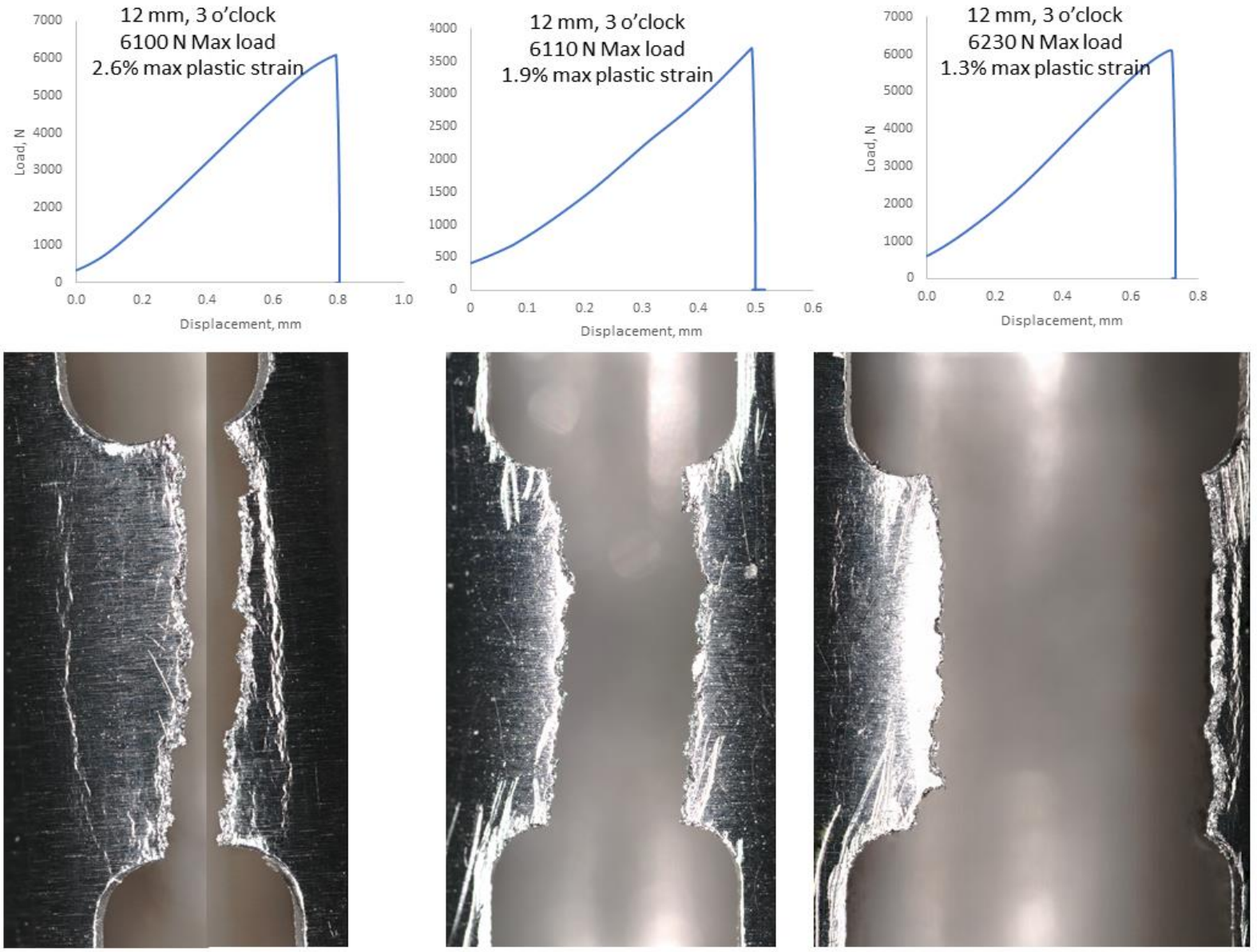

Figure A-5. Gage shape and mechanical test data for 12 mm C26M specimens tested at the 3 o'clock orientation.

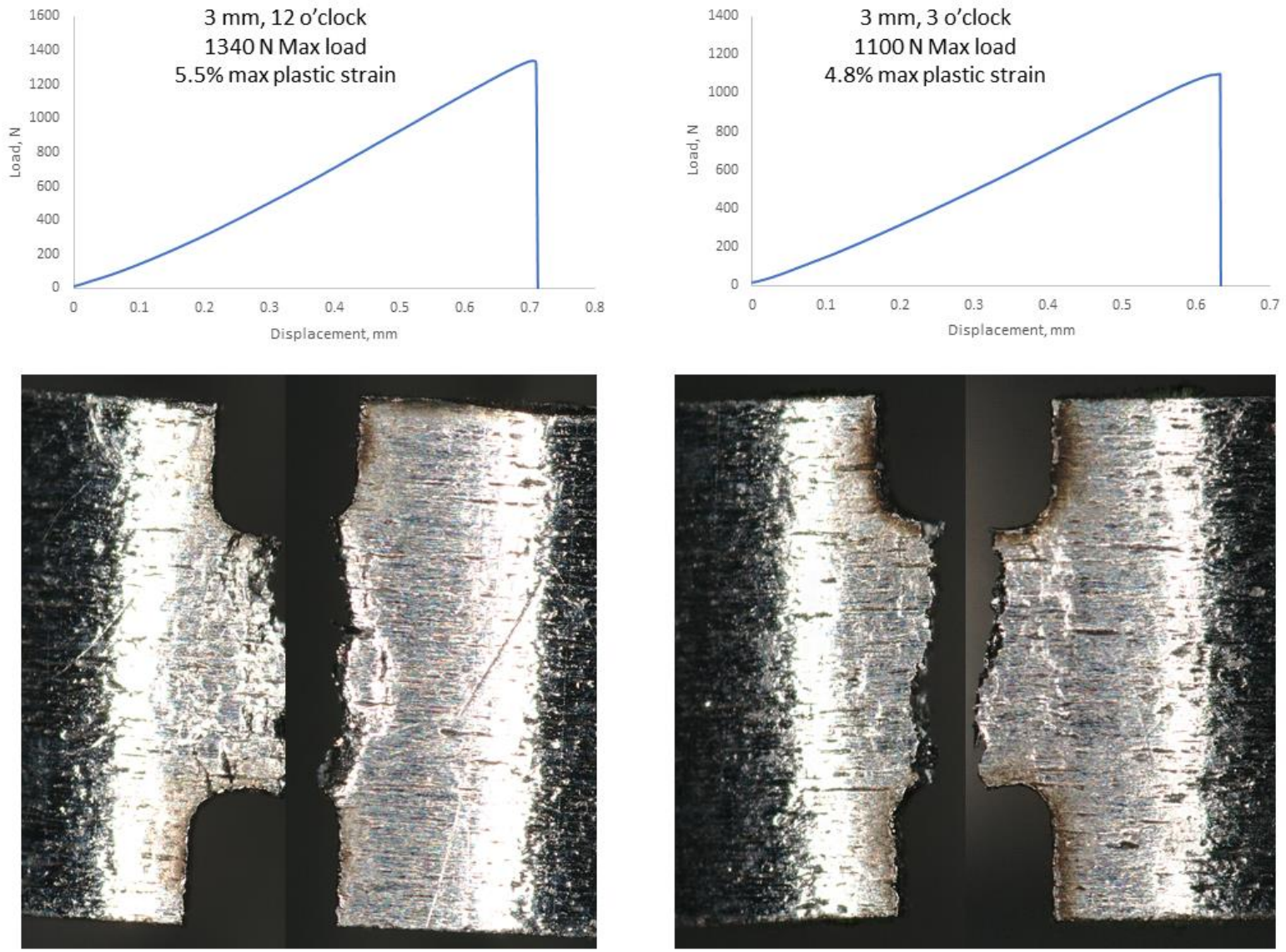

Figure A-6. Gage shape and mechanical test data for 3 mm B136Y specimens tested at the 12 o'clock (left) and 3 o'clock (right) orientations.

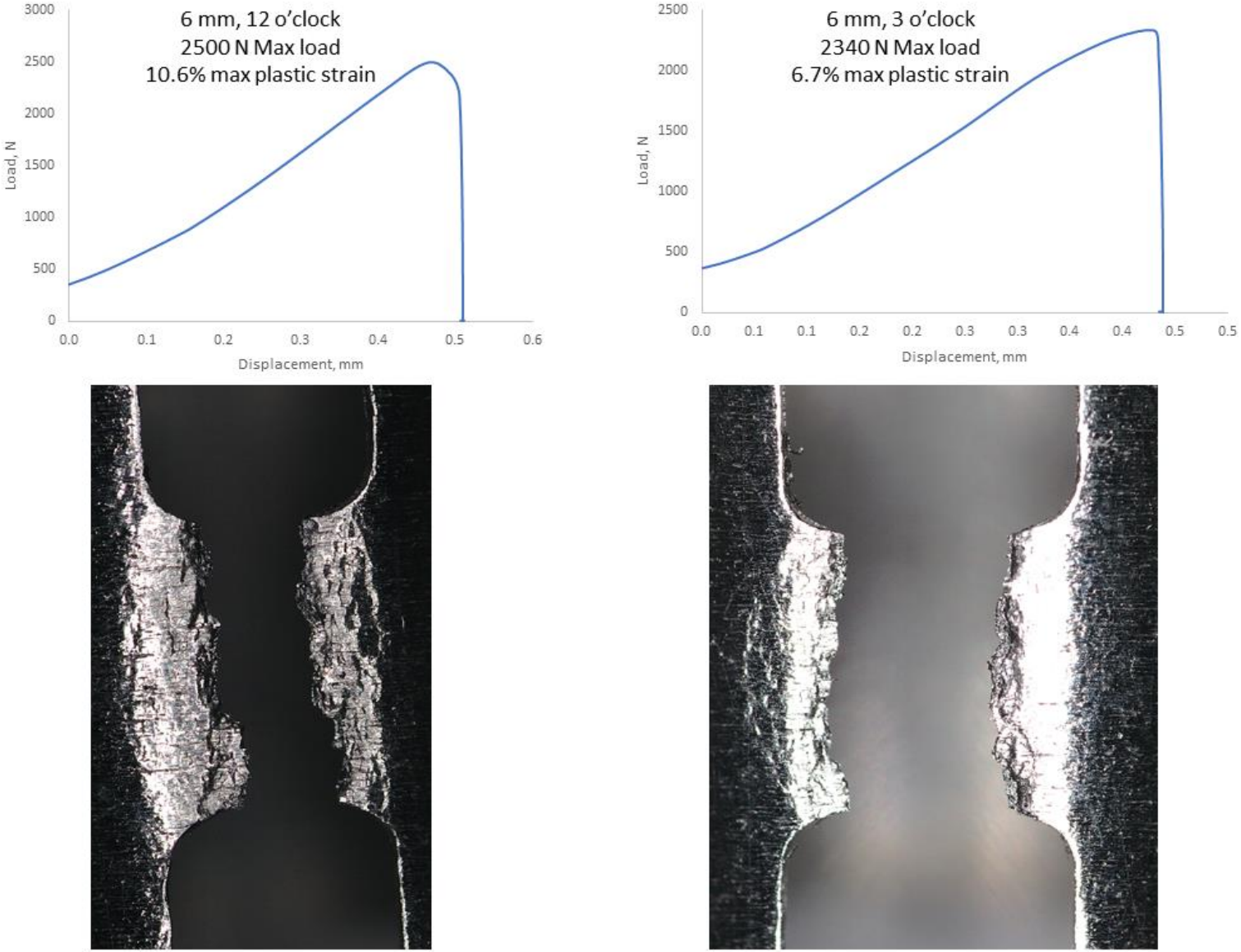

Figure A-7. Gage shape and mechanical test data for 6 mm B136Y specimens tested at the 12 o'clock (left) and 3 o'clock (right) orientations.

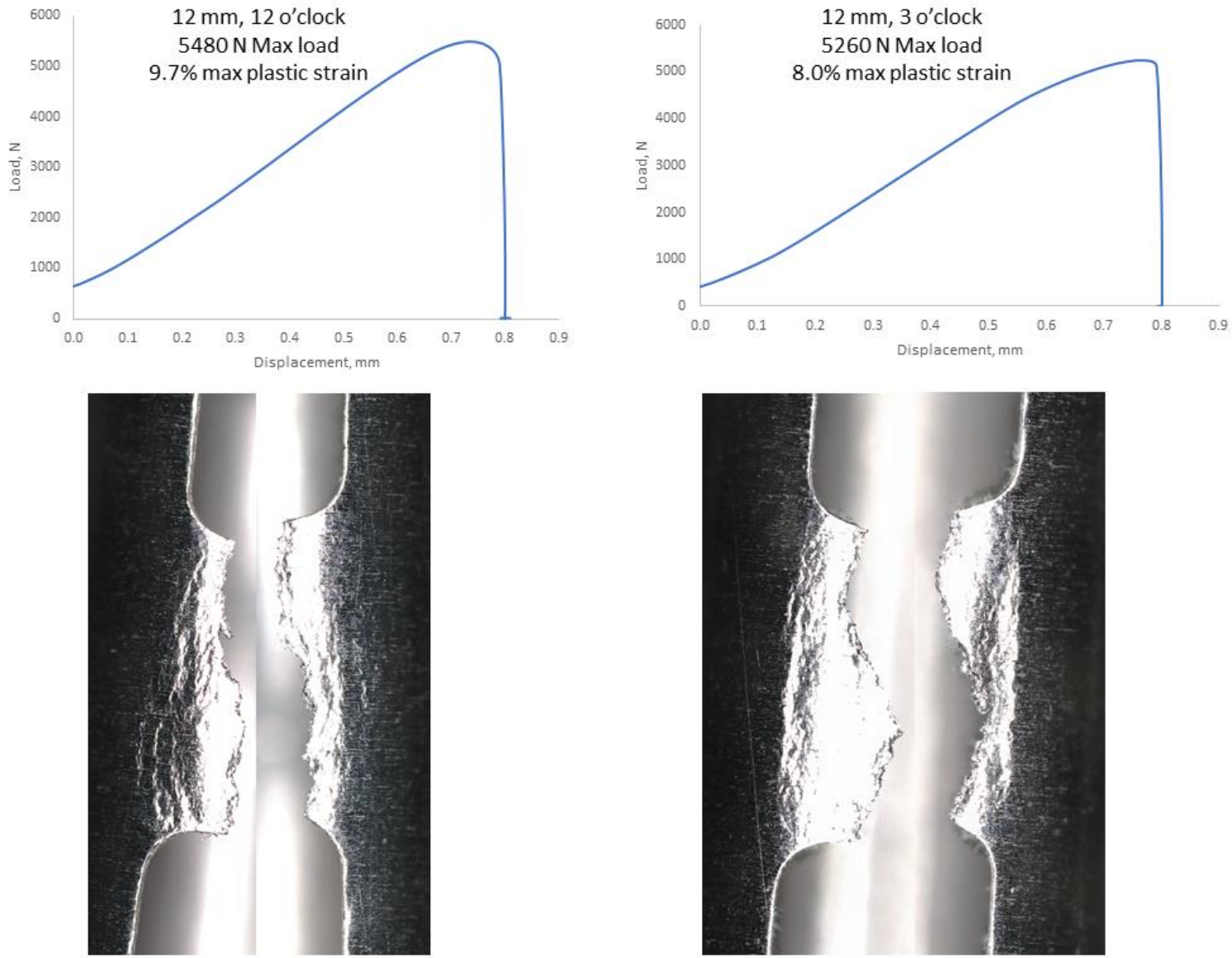

Figure A-8. Gage shape and mechanical test data for 12 mm B136Y specimens tested at the 12 o'clock (left) and 3 o'clock (right) orientations.

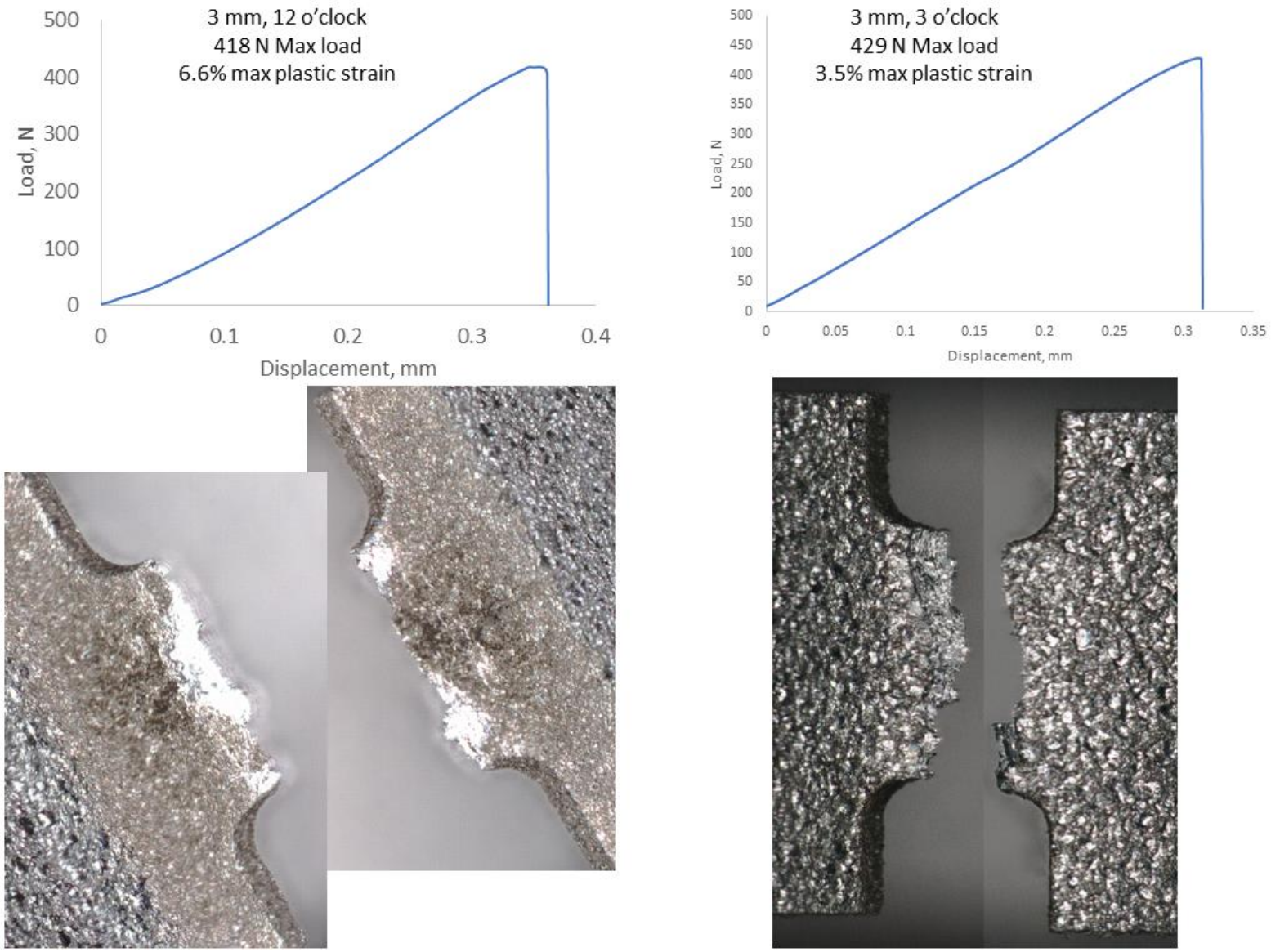

Figure A-9. Gage shape and mechanical test data for 3 mm Al 6061 specimens tested at the 12 o'clock (left) and 3 o'clock (right) orientations.

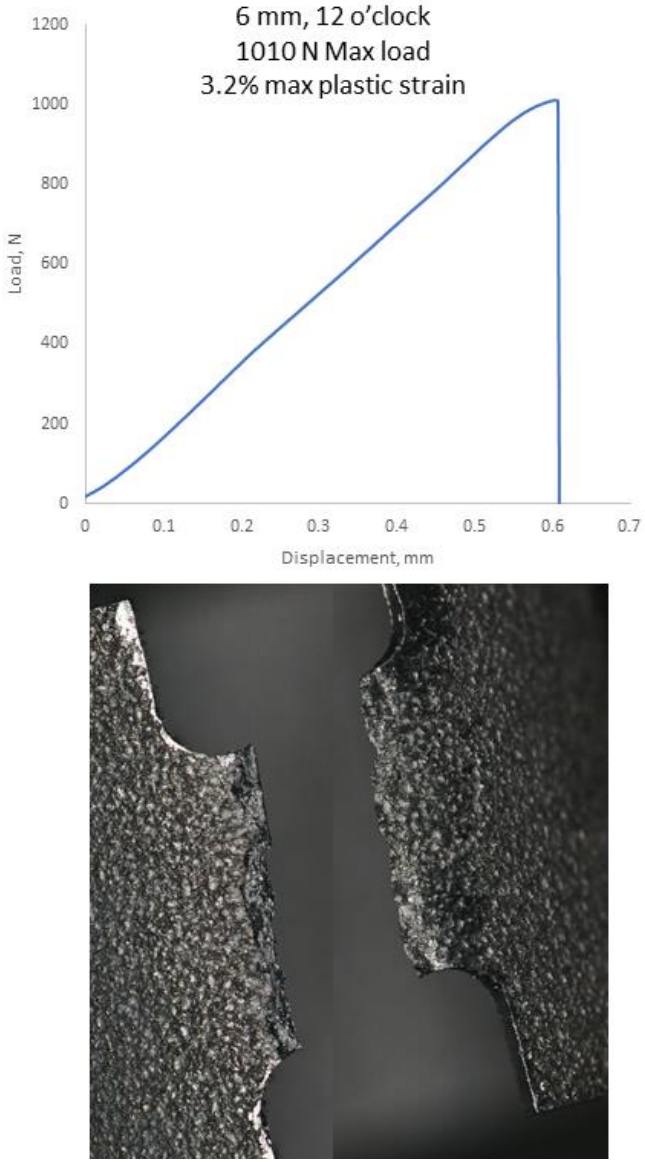

Figure A-10. Gage shape and mechanical test data for 6 mm Al 6061 specimens tested at the 12 o'clock orientation.

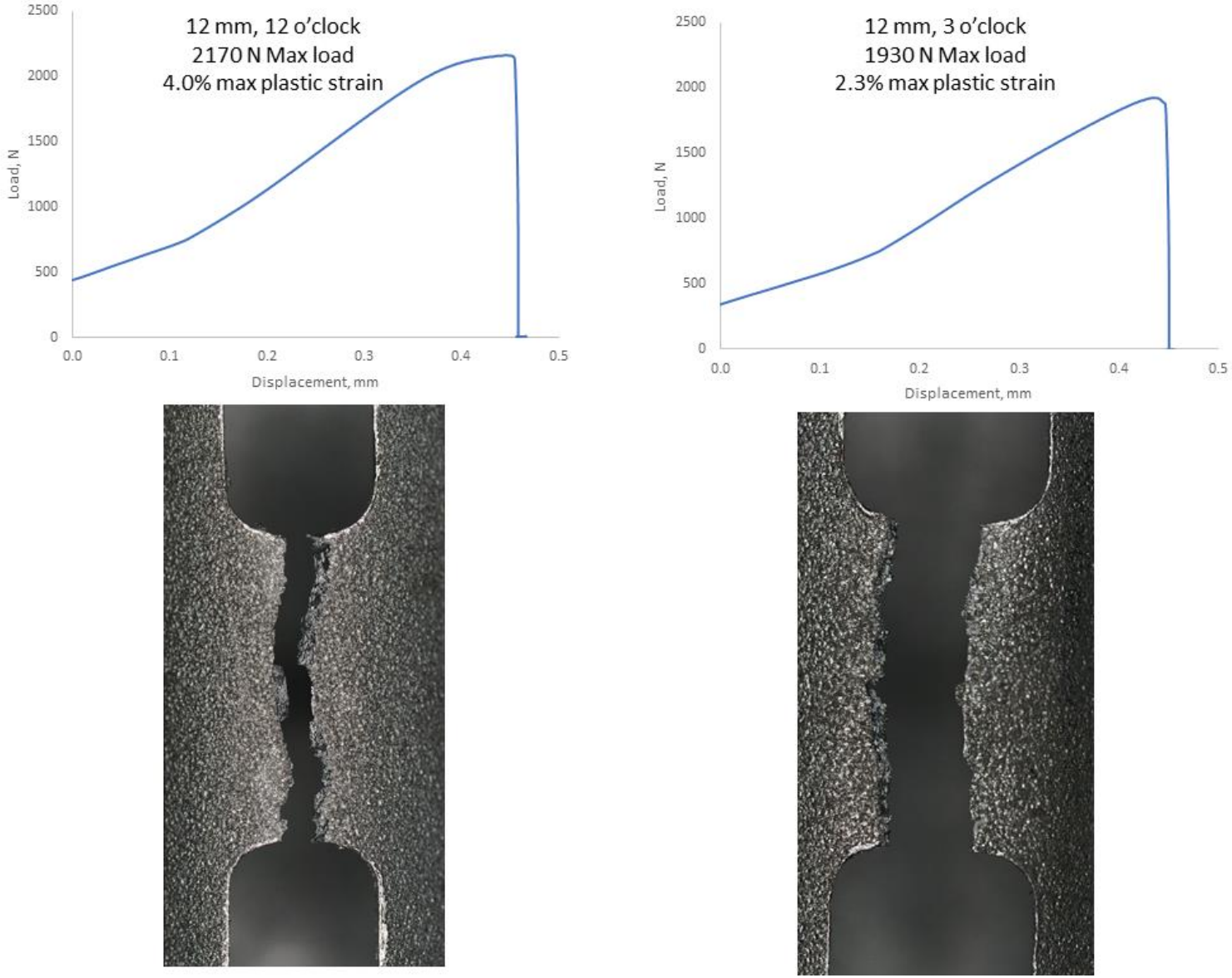

Figure A-11. Gage shape and mechanical test data for 12 mm Al 6061 specimens tested at the 12 o'clock orientation (left) and the 3 o'clock orientation (right).